

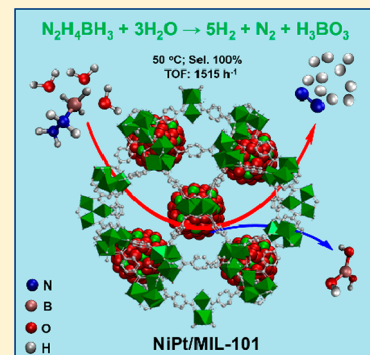
Controlled Synthesis of MOF-Encapsulated NiPt Nanoparticles toward Efficient and Complete Hydrogen Evolution from Hydrazine Borane and Hydrazine

Zhujun Zhang, Shiliang Zhang, Qilu Yao, Xiangshu Chen, and Zhang-Hui Lu*[✉]

Institute of Advanced Materials, College of Chemistry and Chemical Engineering, Jiangxi Normal University, Nanchang 330022, China

Supporting Information

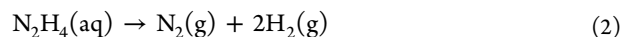
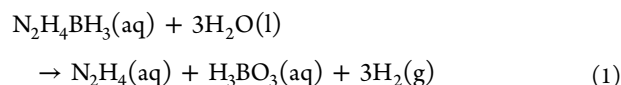
ABSTRACT: The catalytic dehydrogenation of hydrazine borane ($\text{N}_2\text{H}_4\text{BH}_3$) and hydrous hydrazine ($\text{N}_2\text{H}_4\cdot\text{H}_2\text{O}$) for H_2 evolution is considered as two of the pivotal reactions for the implementation of the hydrogen-based economy. A reduction rate controlled strategy is successfully applied for the encapsulating of uniform tiny NiPt alloy nanoclusters within the opening porous channels of MOFs in this work. The resultant $\text{Ni}_{0.9}\text{Pt}_{0.1}/\text{MOF}$ core-shell composite with a low Pt content exerted exceedingly high activity and durability for complete H_2 evolution (100% hydrogen selectivity) from alkaline $\text{N}_2\text{H}_4\text{BH}_3$ and $\text{N}_2\text{H}_4\cdot\text{H}_2\text{O}$ solution. The features of small NiPt alloy NPs, strong synergistic effect between NiPt alloy NPs and the MOF, and open pore structure for freely mass transfer made NiPt/MIL-101 an excellent catalyst for highly efficient H_2 evolution from $\text{N}_2\text{H}_4\text{BH}_3$ or $\text{N}_2\text{H}_4\cdot\text{H}_2\text{O}$.



1. INTRODUCTION

Hydrogen is generally regarded as one of the cleanest and most reliable energy resources because it has high energy capacity ($143 \text{ MJ}\cdot\text{kg}^{-1}$) and is environmentally friendly.^{1–4} However, the implementation of the H_2 -based economy is still hindered by the lack of reliable and efficient hydrogen storage and evolution technology.^{5–7} Hydrazine borane ($\text{N}_2\text{H}_4\text{BH}_3$) is a B–N compound with qualities of high hydrogen content (15.4 wt %) and the potential of 100% hydrogen utilization efficiency and thus has been proposed as a potential hydrogen storage medium.^{8–12} The hydrogen atoms of $\text{N}_2\text{H}_4\text{BH}_3$ can be completely converted to H_2 from the BH_3 group hydrolysis (eq 1) and the N_2H_4 moiety decomposition (eq 2).^{13–21} To achieve a 100% hydrogen utilization efficiency of $\text{N}_2\text{H}_4\text{BH}_3$ as a hydrogen storage media, the incomplete and undesired product of NH_3 from decomposition of N_2H_4 via eq 3 should be avoided. Though much effort has been invested, the catalytic dehydrogenation of hydrazine borane for H_2 evolution is still characterized by significant challenges. To fully dehydrogenate $\text{N}_2\text{H}_4\text{BH}_3$, the catalysts adopted should be both active and selective for the hydrolysis (eq 1) and decomposition process (eq 2). Thus far, most reported catalysts are only effective for the first hydrolysis step,^{13–16} while the selective decomposition of N_2H_4 is still highly dependent on the utilization of noble-metal (Pt and Rh) based catalysts.^{17–29} Noble metal catalysts have received extensive research interest for decades because of their versatility in a variety of areas, especially in catalysis. Although they have incomparable advantages in catalytic activity for chemistry reactions, their high prices and scarcity limitation should be basically considered. In this regard, to maximally enhance their utilization efficiency and meanwhile

harvest high catalytic activity as well as prominent stability for dehydrogenation of $\text{N}_2\text{H}_4\text{BH}_3$ is of fundamental importance.



In general, metal nanoparticles (MNPs) with extremely narrow sizes have exceedingly large surface areas and a great number of edge and corner atoms, which is highly desired for boosting the catalytic properties.^{30,31} However, the increased surface energy of tiny MNPs often leads to their serious aggregation and fusion during a catalytic process, thus resulting in the loss of catalytic activity. Immobilizing metal NPs to porous materials can not only reduce particle aggregation but also control the particle nucleation and growth to the confined pores.³² Besides, the electronic structure and surface state of noble metal can be tailored by alloying with foreign elements, such as transition non-noble metals, which can be beneficial to the adsorption and excitation of reaction substrates and eventually improve the catalytic properties.^{27–29} On the basis of the above consideration, incorporating tiny alloy NPs within porous materials with appropriate pore channels and open windows for mass transfer would be a possible strategy to increase the efficiency and stability of noble metals.

Received: July 26, 2017

Metal–organic frameworks (MOFs) are constructed via the self-assembly of organic linkers and secondary building blocks with tunable and uniform pore structures. The properties of high surface areas and special open pore structure made it an ideal host for the spatial confinement of MNPs.³³ The encapsulating of tiny alloy NPs within the cavities of MOFs would avoid the agglomeration of the confined MNPs, and thus form a stable and accessible structure for freely mass transfer.^{34–40} A facile and general approach that can effectively control the encapsulating of tiny MNPs, especially noble metal based MNPs, within MOFs is significant for practical application.

Herein in this paper, a reduction rate controlled strategy is reported to tailor the size and spatial distribution of NiPt alloy clusters in a MOF crystal as highly efficient catalyst for complete H₂ evolution from alkaline aqueous N₂H₄BH₃ or N₂H₄·H₂O solution. MIL-101(Cr) is selected as the host MOF for NiPt alloy NPs in this work due to its large pore sizes and window sizes, its large specific surface area (up to 5900 m²·g⁻¹), and high thermal (up to 300 °C) and good chemical resistance to water.⁴¹ The MOFs encapsulated tiny NiPt alloy NPs with only 10% Pt (molar ratio: Pt/(Ni + Pt)) exerts exceedingly higher activity than ordinary NiPt alloy NPs for complete dehydrogenation of N₂H₄BH₃ or N₂H₄·H₂O solution for H₂ evolution even at room temperature.

2. EXPERIMENTAL SECTION

2.1. Chemicals and Materials. K₂PtCl₄ (99.95%, Aladdin), NiCl₂·6H₂O (≥98.0%, Sinopharm Chemical Reagent Co., Ltd.), Cr(NO₃)₃·9H₂O (99.95%, Aladdin), NaBH₄ (98%, J&KCHEMICAL), N₂H₄·1/2H₂SO₄ (Sigma-Aldrich), HCl (36–37%, Sinopharm Chemical Reagent Co., Ltd.), HF (37 wt %, J&KCHEMICAL), NaOH (≥96.0%, Sinopharm Chemical Reagent Co., Ltd.), terephthalic acid (HO₂CC₆H₄CO₂H, 99%, Aladdin), 1,4-dioxane (99.8%, J&KCHEMICAL), *n*-pentane (99.5%, Sigma-Aldrich), and ethanol (≥99.7%, Tianjin Fuchen Chemical Reagent) were used as received. The ultrapure water was prepared by reversed osmosis, ion exchange, and filtration.

2.2. Instrumentation. The crystal structure of the synthesized samples was analyzed by powder X-ray diffraction (XRD) with a Rigaku RINT-2200 X-ray diffractometer (Cu K α source, 40 kV, 20 mA). The N₂ adsorption/desorption isotherms at 77 K (liquid nitrogen temperature) were obtained by a BELSORP-mini II. The microstructures and elemental contents of the synthesized samples were analyzed on a transmission electron microscope (TEM, Tecnai G2 F20) and scanning electron microscope (SEM, SU8020 cold field-emission instrument). Inductively coupled plasma atomic emission spectroscopy (ICP-AES, 725-ES) was adopted to detect the detail components of the samples. The surface valence state of the NiPt alloy NPs was determined by X-ray photoelectron spectroscopy (XPS) measurement (Thermo Scientific ESCALAB 250). The evolved gases from dehydrogenation of N₂H₄BH₃ over Ni_{0.9}Pt_{0.1}/MIL-101 catalyst was analyzed by a Balzers Prisma QMS 200 mass spectrometer. ¹H solution-state nuclear magnetic resonance (NMR) was adopted to determine the purity of the synthesized hydrazine borane on a Bruker 400 M liquid ¹H NMR using CD₃CN as solvent.

2.3. Synthesis of NiPt/MIL-101. NiPt/MIL-101_A–C catalysts were synthesized via a general and facile impregnation method combined with a reduction rate controlled strategy. Typically, a solution containing H₂O (5 mL), MIL-101 (50 mg), NiCl₂·6H₂O (0.09 mmol), and K₂PtCl₄ (0.01 mmol) was sonicated for several minutes to get a fully dispersed suspension. Then, the above suspension was vigorously stirred for 8 h at 20 °C to impregnate the metal ions into the pores of the MOF. Finally, NaBH₄ with different NaBH₄/(Ni + Pt) molar ratios (10:1, 7:1, and 4:1) was quickly poured into the above solution, followed by vigorous stirring for 20 min, leading to the generation of a celadon suspension

consisting of Ni_{0.9}Pt_{0.1}/MIL-101_A, Ni_{0.9}Pt_{0.1}/MIL-101_B, and Ni_{0.9}Pt_{0.1}/MIL-101_C, respectively. The preparation of Ni_{1-x}Pt_x/MIL-101_A catalysts ($x = 0, 0.01, 0.04, 0.07, 0.1, 0.13, 0.16, 0.25, 1.0$) with different Pt molar contents follows the similar process for the synthesis of Ni_{0.9}Pt_{0.1}/MIL-101_A catalysts only by adjusting the molar ratio of platinum and nickel salts.

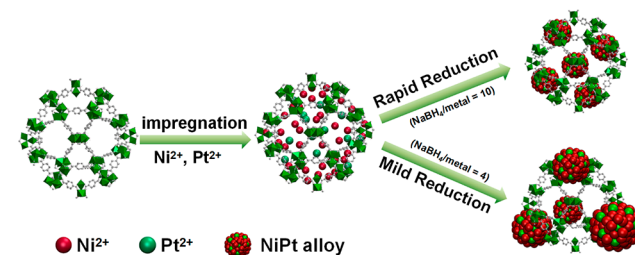
2.4. Catalysis. The catalytic performances of all the samples toward dehydrogenation of N₂H₄BH₃ or N₂H₄·H₂O for H₂ evolution were tested on a water-filled graduated buret system as our previous work reported.^{27–29} Typically, a flask reactor containing the synthesized catalyst suspension and NaOH (0.5 M, 5 mL) was placed in a water bath at a certain temperature. The buret and reactor is connected by a trap filled with HCl solution (0.1 M) to absorb ammonia (NH₃) if generated. The catalytic reaction is started by the injection of N₂H₄BH₃ ((Pt + Ni)/(N₂H₄BH₃) = 0.1) or N₂H₄·H₂O ((Pt + Ni)/(N₂H₄·H₂O) = 0.1) to the above catalyst suspension. Then, the volume of H₂ along with N₂ is measured by the gas buret and recorded at sequential times. Finally, we can calculate the molar ratio $\lambda = n(\text{H}_2 + \text{N}_2)/n(\text{N}_2\text{H}_4\text{BH}_3)$ by the total volume of H₂ and N₂. The hydrogen selectivity for N₂H₄BH₃ dehydrogenation (N₂H₄BH₃ + 3H₂O → B(OH)₃ + (3 + 2 α)H₂ + (2 α + 1)/3N₂ + 4(1 - α)/3NH₃) can be obtained on the basis of the following equation:

$$\alpha = \frac{3\lambda - 10}{8} \left[\lambda = \frac{n(\text{H}_2 + \text{N}_2)}{n(\text{N}_2\text{H}_4\text{BH}_3)} \left(\frac{10}{3} \leq \lambda \leq 6 \right) \right]$$

3. RESULTS AND DISCUSSION

3.1. Synthesis and Characterization of MIL-101 Supported MNPs. A general and facile impregnation method combined with a reduction rate controlled strategy was implemented for the synthesis of MIL-101(Cr) supported NiPt alloy nanoparticles (NPs) with size and location control (Scheme 1). Typically, the Ni²⁺ and Pt²⁺ precursors were first

Scheme 1. Schematic Representation of Preparing MIL-101 Supported NiPt NPs with Size and Location Control



incorporated into the pore channels of MIL-101 via capillary force during an impregnation process. Then, a reduction rate controlled strategy by changing the NaBH₄/(Ni + Pt) molar ratio was applied to obtain the confined NiPt alloy NPs in the MOF with size and location control. The metal precursors deposited inside the MOF can be reduced completely and promptly due to the increase of reduction rate when providing more reducing agent. The instantaneously swelled NiPt NPs can be confined by MOF ligands, and thus the agglomeration of NiPt alloy NPs can be minimized. In contrast, the reduction of metal precursors inside the cages was not timely when providing less reducing agent, thus leading a part of the metal precursors redissolved and diffused to the outside of the pores and aggregated to large metal clusters on the external surface.

The nanocomposites obtained with a NaBH₄/(Ni + Pt) molar ratio of 10:1, 7:1, and 4:1 are named as NiPt/MIL-101_A, NiPt/MIL-101_B, and NiPt/MIL-101_C, respectively.

The typical SEM, TEM, and high-angle annular dark-field scanning TEM (HAADF-STEM) images of the obtained NiPt/MIL-101_A–C catalysts are illustrated in Figure 1. The

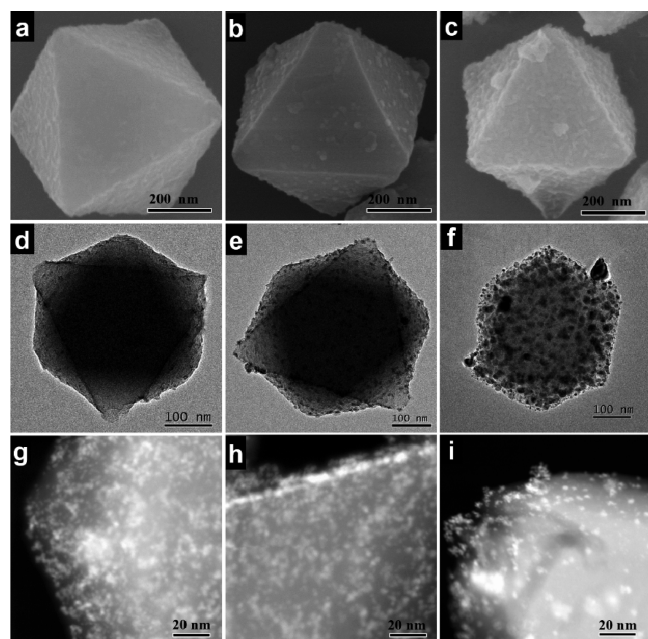


Figure 1. SEM, TEM, and HAADF-STEM images of Ni_{0.9}Pt_{0.1}/MIL-101_A (a, d, g), Ni_{0.9}Pt_{0.1}/MIL-101_B (b, e, h), and Ni_{0.9}Pt_{0.1}/MIL-101_C (c, f, i), respectively.

octahedral framework of MIL-101 (Figure S1) kept complete and uniform after the loading of NiPt NPs via the reduction rate controlled strategy. It can be seen from the SEM (Figure 1a), bright-field TEM (Figure 1d and Figure S2a), and HAADF-STEM images (Figure 1g) that the NiPt NPs obtained through a rapid reduction process (NaBH₄/(Ni + Pt) molar ratio = 10:1) are highly distributed into the framework of MIL-101 (NiPt/MIL-101_A). The mean particle size of the NiPt NPs is 2.5 nm (Figure S2a). As the MOF MIL-101 used in this work has mesoporous cavities with sizes of ~3.2 nm and windows with sizes of ~1.2 and 1.6 nm,⁴¹ it is reasonable that the obtained NiPt NPs (2.5 nm) can be accommodated into the mesoporous cavities confined by the windows. However, larger metal clusters on the surface of the MOF crystal are observed from both the SEM, bright and dark TEM images of NiPt/MIL-101_B and NiPt/MIL-101_C (Figure 1 and Figure S2c,d). For the NiPt/MIL-101_B sample, a part of NiPt NPs with particle sizes of about 4.5 nm are aggregated to large clusters on the surface of the MOF crystal (Figure S2c). When the NaBH₄/(Ni + Pt) molar ratio was further decreased to 4:1, more NiPt NPs with sizes bigger than 5 nm are aggregated together as larger clusters (~25 nm) on the surface of the MIL-101 framework (NiPt/MIL-101_C) (Figure S2d). These results reveal that the reduction rate controlled process is effective to control the size and spatial distribution of NiPt NPs in a MOF framework, which can be easily expanded to the synthesis of other heterogeneous catalysts with similar porous structures. The high-resolution TEM (HRTEM) image of NiPt/MIL-101_A (Figure S2b) confirms the crystalline alloy nature of Ni–Pt NPs, as the *d*-spacing (~0.219 nm) is between the Pt(111) plane (0.227 nm) and the Ni(111) plane (0.203 nm). In addition, the corresponding energy dispersive X-ray detector (EDX) pattern of NiPt/MIL-101_A (Figure S3)

demonstrates the uniformity of NiPt alloy NPs in the Cr-based MOF. The detail composition of the catalysts can be further determined by using the ICP-AES instrument (Table S1).

The parent MIL-101 and NiPt/MIL-101_A–C catalysts with specific surface areas of 2794, 1411, 1533, and 1670 m²·g⁻¹ (Table 1), respectively, are determined by N₂ adsorption/

Table 1. Physical Properties and Activities of Ni_{0.9}Pt_{0.1}/MIL-101_A–C Catalysts Synthesized via a Reduction Rate Controlled Strategy

sample	S _{BET} [m ² g ⁻¹]	D ^a [nm]	size [nm]	TOF ^b [h ⁻¹]
NiPt/MIL-101_A	1411	2.98/1.45/1.05	2.5	1515
NiPt/MIL-101_B	1533	3.00/1.53/1.05	4.5	732
NiPt/MIL-101_C	1670	3.11/1.62/1.05	5–25	500

^aMicropore size obtained by using the QSDFT method (slit/cylindrical pore model). ^bTOF values for dehydrogenation of N₂H₄BH₃ are calculated based on the number of full metal (Ni + Pt) atoms in catalysts.

desorption isotherms measurement using the Brunauer–Emmett–Teller (BET) model (Figure 2a). The pore size of NiPt/MIL-101_A–C is slightly smaller than that of the parent MIL-101 (Figure 2b). The decrease in N₂ sorption and pore sizes compared with the parent MIL-101 is probably because the cavities are occupied by the NiPt alloy NPs. The N₂ sorption capacity of NiPt/MIL-101_A is a little lower than that of NiPt/MIL-101_B and C, which is probably due to that more metal NPs are deposited inside the pore channels after a rapid reduction process. The low-angle XRD patterns show no crystallinity loss for the MOF after the formation of NiPt/MIL-101 catalysts (Figure 2c), further demonstrating the integrity of the MIL-101 crystal during the catalyst synthesis process. It can be seen from the wide-angle powder XRD patterns that both NiPt/MIL-101_B and C composites exhibit a weak and broad peak at around 2θ = 41.8°, which is between the characteristic peaks for Pt(111) (PDF# 05-0685) and Ni(111) (PDF# 04-0850) (Figure 2d), verifying the nanoalloy structure of NiPt NPs. In comparison with NiPt/MIL-101_B and NiPt/MIL-101_C samples, NiPt/MIL-101_A has a unobvious NiPt alloy signal due to its smaller particle sizes inside the MOF. X-ray photoelectron spectroscopic (XPS) measurement on the NiPt/MIL-101_A with Ar sputtering was carried out to determine the surface valence state of the metal NPs (Figure 3). The Ni species are present in both the oxide and the metallic forms. The binding energies (BEs) at 852.8 and 870.2 eV that are attributed to Ni⁰ could be detected after the thin oxidized layer was eliminated by Ar sputtering in 60 s. Meanwhile, the characteristic signals of Pt 4f centered at binding energies (BEs) of around 70.6 and 73.9 eV can be assigned to Pt⁰.

3.2. Catalytic Performance. The obtained NiPt/MIL-101_A catalysts with different molar contents of Pt have been tested for the catalytic dehydrogenation of alkaline N₂H₄BH₃ solution (0.5 M NaOH) at 323 K as shown in Figure 4. NaOH was used to promote the decomposition of N₂H₄.^{27–30} The optimum concentration of NaOH for dehydrogenation of N₂H₄BH₃ was measured to be 0.5 M in the present reaction system (Figure S4). Obviously, both the monometallic Ni/MIL-101_A and Pt/MIL-101_A catalysts showed a certain activity for H₂ evolution from the BH₃ group hydrolysis and the

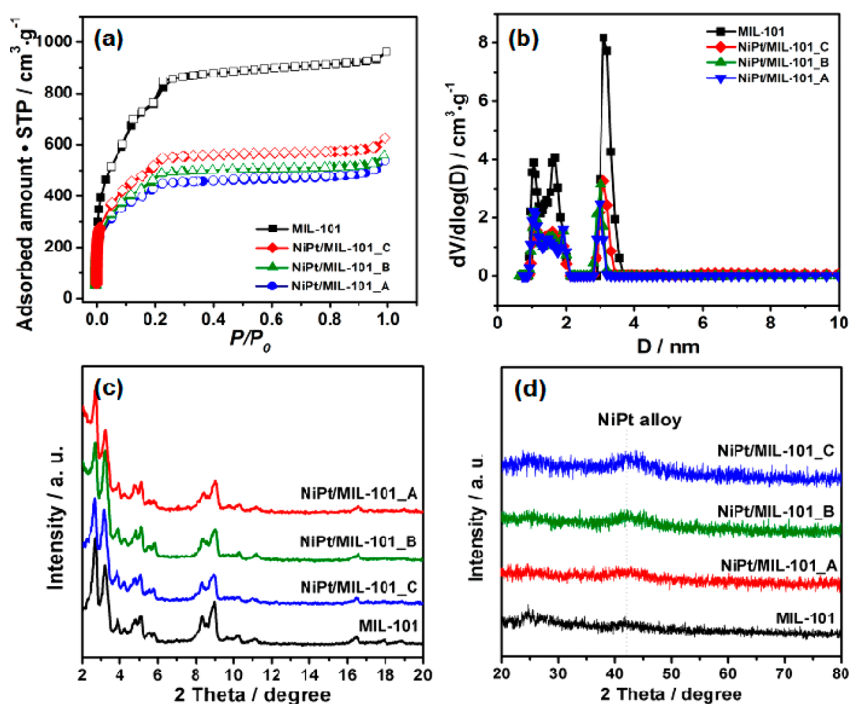


Figure 2. (a) N₂ sorption isotherms, (b) the pore size distribution curves, (c) the low-angle and (d) wide-angle powder XRD patterns for the as-synthesized MIL-101, Ni_{0.9}Pt_{0.1}/MIL-101_A, Ni_{0.9}Pt_{0.1}/MIL-101_B, and Ni_{0.9}Pt_{0.1}/MIL-101_C.

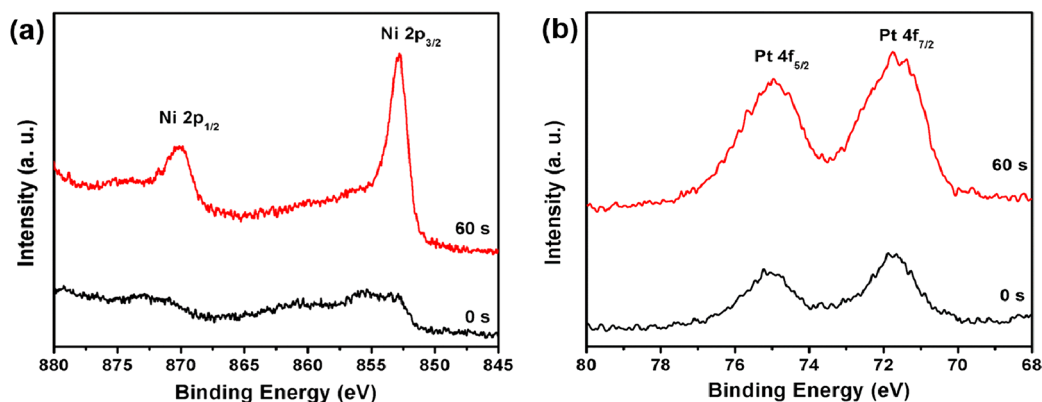


Figure 3. XPS spectra of the electron binding energies for (a) Ni 2p and (b) Pt 4f in the Ni_{0.9}Pt_{0.1}/MIL-101_A catalyst before (0 s) and after argon sputtering for 60 s.

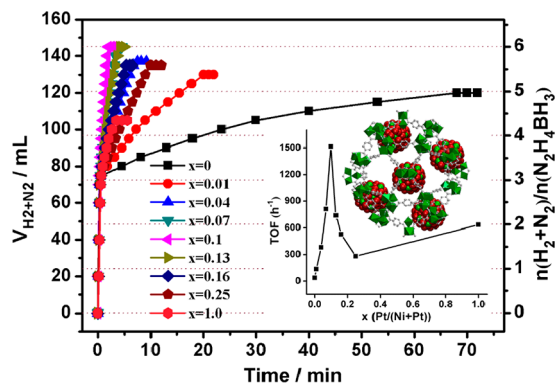


Figure 4. Time course plots for H₂ generation from alkaline aqueous N₂H₄BH₃ solution (1.0 mmol, 5.0 mL, 0.5 M NaOH) at 323 K catalyzed by the Ni_{1-x}Pt_x/MIL-101_A. Inset: the corresponding TOF values of the catalysts with different Pt molar contents and the simulated diagram of NiPt/MIL-101_A.

N₂H₄ moiety decomposition with a total of 4.97 and 4.34 equiv (H₂ + N₂) per N₂H₄BH₃ released in 68 and 3.6 min, respectively. The activity and H₂ selectivity for the N₂H₄ moiety decomposition were significantly increased by Ni-Pt alloying with a very little amount of Pt (Figure 4). The bimetallic NiPt/MIL-101_A catalysts with low Pt contents of 7–13 mol % showed 100% H₂ selectivity and excellent activity (Figure 4). Among them, the best catalytic performance is observed for the Ni_{0.9}Pt_{0.1}/MIL-101_A sample, with which the reaction was completed in only 1.92 min, which corresponds to a total turnover frequency (TOF) of 1515 mol_{H₂}·mol_(Ni+Pt)⁻¹·h⁻¹ (inset of Figure 4). This is 84-fold higher than that of the reported catalyst Ni_{0.89}Pt_{0.11} NPs stabilized by CTAB (Table S2).²² Further increase or decrease of Pt content in NiPt/MIL-101_A catalyst leads to the decrease of catalytic activity and H₂ productivity, suggesting the Ni_{0.9}Pt_{0.1}/MIL-101_A with a Ni:Pt molar ratio of 9:1 can optimize the synergy between Ni and Pt based on their electronic and geometric effects in the present

reaction conditions. The H_2/N_2 ratio of the evolved gases from dehydrogenation of $N_2H_4BH_3$ over $Ni_{0.9}Pt_{0.1}/MIL-101_A$ catalyst was determined by mass spectrometric analysis (Figure S5), indicating the 100% H_2 selectivity.

For comparison, the parent MIL-101 and $Ni_{0.9}Pt_{0.1}$ NPs were separately applied to the dehydrogenation of $N_2H_4BH_3$ at the same conditions. Obviously, only 5.4 equiv ($H_2 + N_2$) per $N_2H_4BH_3$ was released in more than 40 min by $Ni_{0.9}Pt_{0.1}$ NPs, while MIL-101 was inactive (Figure 5). The $Ni_{0.9}Pt_{0.1}/MIL-$

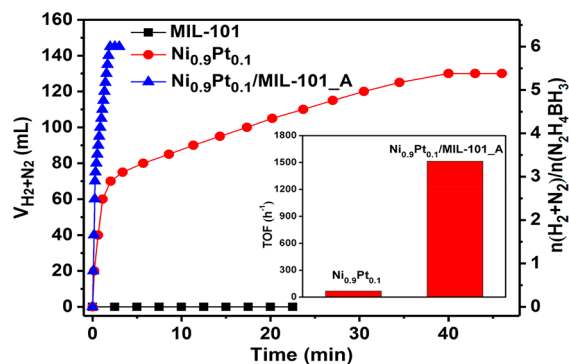


Figure 5. Time course plots for H_2 generation from alkaline aqueous $N_2H_4BH_3$ solution (1.0 mmol, 5.0 mL, 0.5 M NaOH) at 323 K catalyzed by the parent MIL-101, the $Ni_{0.9}Pt_{0.1}$ NPs, and $Ni_{0.9}Pt_{0.1}/MIL-101_A$. Inset: The corresponding TOF values of $Ni_{0.9}Pt_{0.1}$ and $Ni_{0.9}Pt_{0.1}/MIL-101_A$, respectively.

101_A shows a marked, more than 21-fold increase in activity and a much higher selectivity compared with the parent $Ni_{0.9}Pt_{0.1}$ NPs (that is, TOF of $68 h^{-1}$ and selectivity of 77.5%) (inset of Figure 5). Thus, the strong interaction of the MOF crystal and Ni-Pt alloy NPs is highly required for the better catalytic performance. Due to the multiple advantages of the synthesized $Ni_{0.9}Pt_{0.1}/MIL-101_A$ catalyst, namely, the smaller particle sizes of NiPt alloy NPs provide more active sites, the enrichment of substrates inside the pores of the MOF highly boost the adsorption of $N_2H_4BH_3$ by the active sites, and the open pore structure of the catalyst endows the freely mass transfer in and out of catalysts during the heterogeneous catalytic process, the greatly enhanced catalytic performance

can be achieved. It is also found that both the $NiPt/MIL-101_B$ and C catalysts, which were synthesized via a mild reduction process, display high catalytic activity for H_2 evolution from dehydrogenation of $N_2H_4BH_3$ with a total TOF value of 732 and $500 h^{-1}$, respectively (Figure 6). However, their catalytic activities were still much lower than that of $NiPt/MIL-101_A$ catalyst ($1515 h^{-1}$). The NiPt alloy NPs in $NiPt/MIL-101_A$ have smaller particle sizes and the confined active sites in the pore channels of MOF are more accessible than that of the aggregated one in the outer surface of MOF. The enhanced catalytic activity of $NiPt/MIL-101_A$ may mostly due to its smaller NiPt particle sizes encapsulated in the pores of the MOF and stronger interaction between bimetallic NPs and the MOF matrix.

The catalytic activity of $Ni_{0.9}Pt_{0.1}/MIL-101_A$ has also been tested for dehydrogenation of $N_2H_4BH_3$ at different temperatures. The reactions were completed in 1.42, 1.95, 3.67, and 7.50 min at temperatures ranging from 333, 323, 313, and 303 K, corresponding to total TOF values of 2113, 1515, 817, and $400 mol_{H_2} \cdot mol_{(Ni+Pt)}^{-1} \cdot h^{-1}$, respectively (Figure 7a). It should be noted that $Ni_{0.9}Pt_{0.1}/MIL-101_A$ has a tremendously high TOF value even at room temperature. The TOF value evaluated by the noble-metal content reaches $4000 mol_{H_2} \cdot mol_{Pt}^{-1} \cdot h^{-1}$, which is much higher than that of MSC-30 supported $Ni_{0.6}Pt_{0.4}$ NPs (TOF: $1667 mol_{H_2} \cdot mol_{Pt}^{-1} \cdot h^{-1}$), the best catalyst reported so far at room temperature.²⁵ The highly efficient utilization of noble metal endows this catalyst with more possibility for practical application. The activation energy value for hydrolysis of the BH_3 group (Part 1 in Figure 7a) and decomposition of the N_2H_4 moiety (Part 2 in Figure 7a) of $N_2H_4BH_3$ over $Ni_{0.9}Pt_{0.1}/MIL-101_A$ can be estimated to be 18.6 and 44.6 kJ/mol, respectively, by using the Arrhenius plot fitted by the corresponding H_2 generation rate at different reaction temperatures (Figure 7b).

Hydrous hydrazine is a promising liquid hydrogen storage material with high hydrogen content.^{42–45} The complete decomposition (100% selectivity calculated by Eq S1) of $N_2H_4 \cdot H_2O$ over $Ni_{0.9}Pt_{0.1}/MIL-101_A$ at 333, 323, 313, and 303 K can be finished in 1.3, 1.9, 4.1, and 8.6 min, corresponding to total TOF values of 922, 621, 296, and 140

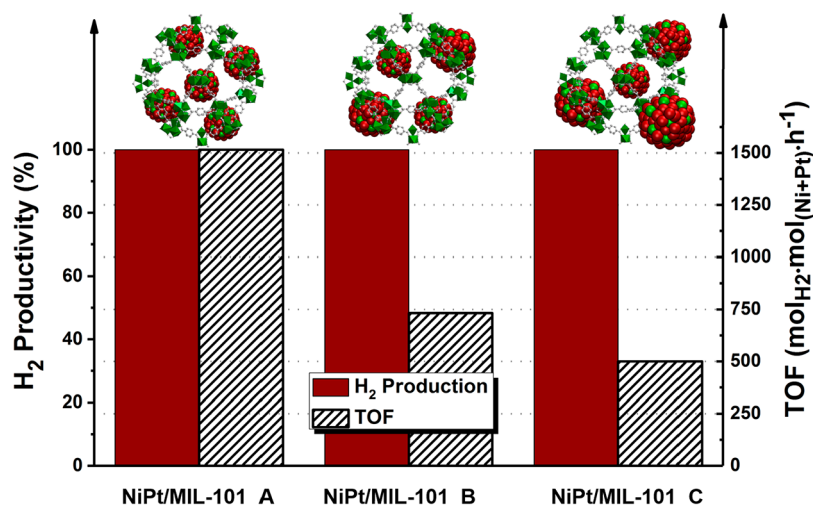


Figure 6. Catalytic performance of $Ni_{0.9}Pt_{0.1}/MIL-101$ catalysts with different active sites locations for H_2 generation from alkaline aqueous $N_2H_4BH_3$ solution (1.0 mmol, 5.0 mL, 0.5 M NaOH). Inset: the corresponding simulated diagrams of different $Ni_{0.9}Pt_{0.1}/MIL-101$ catalysts.

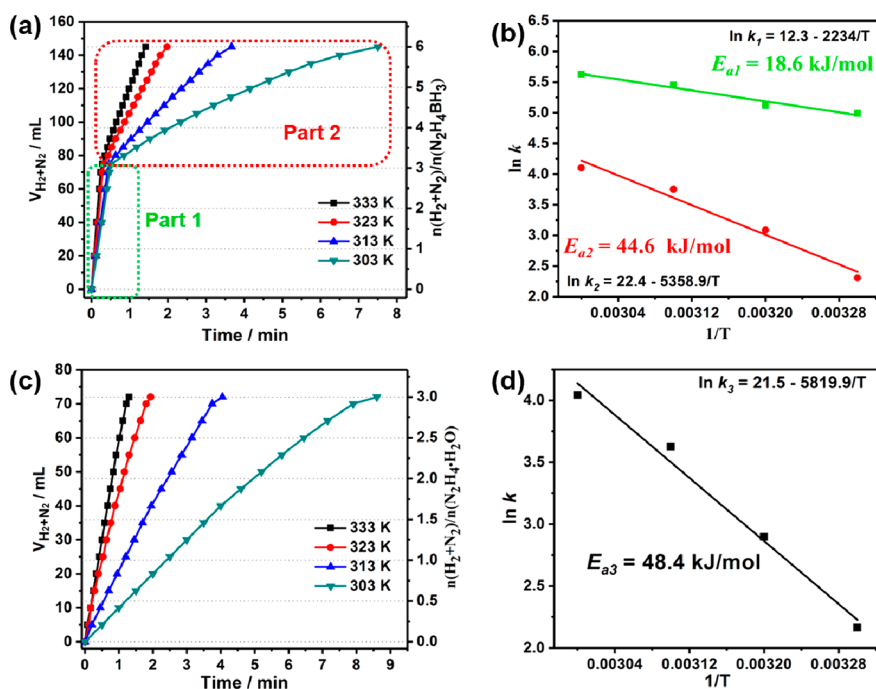


Figure 7. (a) Time course plots for H₂ generation from aqueous solution of N₂H₄BH₃ and (c) N₂H₄·H₂O over Ni_{0.9}Pt_{0.1}/MIL-101_A catalyst at temperatures ranging from 303 to 333 K. Plot of ln *k* versus 1/*T* during the releasing of H₂ from (b) the hydrolysis of BH₃ group (Part 1) and decomposition of the N₂H₄ moiety (Part 2) and (d) decomposition of N₂H₄·H₂O over Ni_{0.9}Pt_{0.1}/MIL-101_A catalyst at different temperatures.

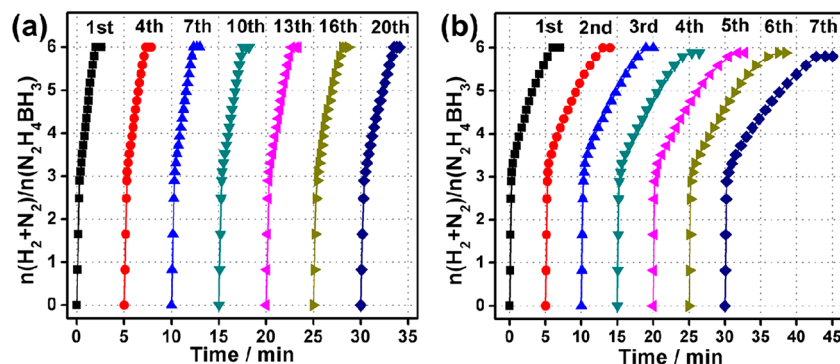


Figure 8. Durability test for the H₂ generation from alkaline aqueous N₂H₄BH₃ solution catalyzed by Ni_{0.9}Pt_{0.1}/MIL-101_A (a) and Ni_{0.9}Pt_{0.1}/MIL-101_C (b) at 323 K.

mol_{H₂}·mol_(Ni+Pt)⁻¹·h⁻¹, respectively. The activation energy value for decomposition of N₂H₄·H₂O is estimated to be 48.4 kJ/mol (Figure 7c,d), a little higher than that for decomposition of the N₂H₄ moiety of N₂H₄BH₃.⁴⁶ These TOF and activation energy values are comparable to those of state-of-the-art catalysts (Table S3). The NiPt/MIL-101_A showed a little higher catalytic activity for H₂ evolution from N₂H₄BH₃ than that from N₂H₄·H₂O. A plausible explanation is that the quick hydrolysis of the BH₃ group of N₂H₄BH₃ (Figure 7a,b) can highly accelerate the transfer of the resulting N₂H₄ moiety to the active sites and promote the kinetic for decomposition of N₂H₄.

The stability of a catalyst is of great importance for practical application. Therefore, the durability of the Ni_{0.9}Pt_{0.1}/MIL-101_A catalyst for H₂ evolution from dehydrogenation of N₂H₄BH₃ at 323 K was tested (Figure 8a). After 20 cycles of reactions, the H₂ productivity was kept at 100% with a slight decrease in catalytic activity, indicating that the Ni_{0.9}Pt_{0.1}/MIL-101_A catalyst has prominent durability in catalytic dehydro-

genation of N₂H₄BH₃ as well as in decomposition of N₂H₄·H₂O (Figure S6). Without the stabilization of MOF ligands, the NiPt NPs on the outer surface of Ni_{0.9}Pt_{0.1}/MIL-101_C turned to be easily aggregated after reaction (Figure S7). The MOF frameworks of Ni_{0.9}Pt_{0.1}/MIL-101_A were not well retained during the durability test according to the SEM image and XRD pattern of the sample after 7 cycles of reactions in dehydrogenation of N₂H₄BH₃ (Figures S8 and S9), probably due to the long-time corrosion by high concentration of NaOH in the reaction solution. However, the micropore and mesopore features of MOF were well retained as verified by the corresponding N₂ sorption isotherms (Figure S10a) and pore size distribution curves (Figure S10b). From the TEM and HAADF-STEM images of the sample after 20 cycles of reactions in dehydrogenation of N₂H₄BH₃, the NiPt alloy NPs are still highly dispersed in the resulting fragments and the serious aggregation of metal NPs is not observed (Figure S11). Consequently, we believe that the favorable activity of NiPt/MIL-101_A retained during the durability test in dehydro-

ation of alkaline $N_2H_4BH_3$ (Figure 8a) or $N_2H_4 \cdot H_2O$ (Figure S6) is mainly due to the fact that the ligands of MIL-101 can avoid the particle aggregation during the heterogeneous catalytic process.

4. CONCLUSION

In summary, a series of catalysts that comprise tiny NiPt alloy NPs encapsulated within a MOF have been successfully synthesized via a reduction rate controlled strategy, which is proved to be effective to tailor the size and spatial distribution of bimetallic alloy NPs in porous materials. When a rapid reduction process with a higher $NaBH_4$ /metals molar ratio was applied, most of the bimetallic NiPt alloy NPs with a tiny size (2.5 nm) would be encapsulated within the pore channels of MOFs without agglomeration on the external surface of the host. The resulting low Pt content $Ni_{0.9}Pt_{0.1}/MIL-101$ A catalyst exhibited outstanding activity and durability for complete H_2 evolution from dehydrogenation of $N_2H_4BH_3$ or $N_2H_4 \cdot H_2O$ and, thus, may promote the practical use of $N_2H_4BH_3$ and $N_2H_4 \cdot H_2O$ as chemical hydrogen storage materials for H_2 evolution. The MOF ligands stabilized NiPt NPs displayed excellent durability in 20 cycles of reactions without obvious activity loss and MNPs aggregation, though the MOF frameworks were not well retained during the long-time corrosion by high concentration of NaOH in the reaction solution.

■ ASSOCIATED CONTENT

Supporting Information

The Supporting Information is available free of charge on the ACS Publications website at DOI: 10.1021/acs.inorgchem.7b01910.

Additional information as noted in text (PDF)

■ AUTHOR INFORMATION

Corresponding Author

*E-mail: luzh@jxnu.edu.cn.

ORCID

Zhang-Hui Lu: 0000-0001-6342-0879

Notes

The authors declare no competing financial interest.

■ ACKNOWLEDGMENTS

This work was financially supported by the National Natural Science Foundation of China (Nos. 21763012 and 21463012) and the Natural Science Foundation of Jiangxi Province of China (Nos. 20171ACB21021 and 2016BAB203087).

■ REFERENCES

- (1) He, T.; Pachfule, P.; Wu, H.; Xu, Q.; Chen, P. Hydrogen carriers. *Nat. Rev. Mater.* **2016**, *1*, 16059.
- (2) Graetz, J. New approaches to hydrogen storage. *Chem. Soc. Rev.* **2009**, *38*, 73–82.
- (3) Yao, Q.; Shi, W.; Feng, G.; Lu, Z.-H.; Zhang, X.; Tao, D.; Kong, D.; Chen, X. Ultrafine Ru nanoparticles embedded in SiO_2 nanospheres: Highly efficient catalysts for hydrolytic dehydrogenation of ammonia borane. *J. Power Sources* **2014**, *257*, 293–299.
- (4) Lu, Z.-H.; Li, J.; Zhu, A.; Yao, Q.; Huang, W.; Zhou, R.; Chen, X.; Zhou, R. Catalytic hydrolysis of ammonia borane via magnetically recyclable copper iron nanoparticles for chemical hydrogen storage. *Int. J. Hydrogen Energy* **2013**, *38*, 5330–5337.
- (5) Zhu, Q.-L.; Xu, Q. Liquid organic and inorganic chemical hydrides for high-capacity hydrogen storage. *Energy Environ. Sci.* **2015**, *8*, 478–512.
- (6) Yang, J.; Sudik, A.; Wolverton, C.; Siegel, D. J. High capacity hydrogen storage materials: attributes for automotive applications and techniques for materials discovery. *Chem. Soc. Rev.* **2010**, *39*, 656–675.
- (7) Sevilla, M.; Mokaya, R. Energy storage applications of activated carbons: supercapacitors and hydrogen storage. *Energy Environ. Sci.* **2014**, *7*, 1250–1280.
- (8) Hügle, T.; Kühnel, M. F.; Lentz, D. Hydrazine borane: a promising hydrogen storage material. *J. Am. Chem. Soc.* **2009**, *131*, 7444–7446.
- (9) Goubeau, J.; Ricker, E. Borinhydrazin und seine pyrolyseprodukte. *Z. Anorg. Allg. Chem.* **1961**, *310*, 123–142.
- (10) He, T.; Wu, H.; Wu, G.; Wang, J.; Zhou, W.; Xiong, Z.; Chen, J.; Zhang, T.; Chen, P. Borohydride hydrazinates: high hydrogen content materials for hydrogen storage. *Energy Environ. Sci.* **2012**, *5*, 5686–5689.
- (11) Wu, H.; Zhou, W.; Pinkerton, F. E.; Udovic, T. J.; Yildirim, T.; Rush, J. J. Metal hydrazinoborane $LiN_2H_3BH_3$ and $LiN_2H_3BH_3 \cdot 2N_2H_4BH_3$: crystal structures and high-extent dehydrogenation. *Energy Environ. Sci.* **2012**, *5*, 7531–7535.
- (12) Moury, R.; Moussa, G.; Demirci, U. B.; Hannauer, J.; Bernard, S.; Petit, E.; van der Lee, A.; Miele, P. Hydrazine borane: synthesis, characterization, and application prospects in chemical hydrogen storage. *Phys. Chem. Chem. Phys.* **2012**, *14*, 1768–1777.
- (13) Karahan, S.; Zahmakiran, M.; Özkaz, S. Catalytic hydrolysis of hydrazine borane for chemical hydrogen storage: Highly efficient and fast hydrogen generation system at room temperature. *Int. J. Hydrogen Energy* **2011**, *36*, 4958–4966.
- (14) Hannauer, J.; Demirci, U. B.; Geantet, C.; Herrmann, J.-M.; Miele, P. Transition metal-catalyzed dehydrogenation of hydrazine borane $N_2H_4BH_3$ via the hydrolysis of BH_3 and the decomposition of N_2H_4 . *Int. J. Hydrogen Energy* **2012**, *37*, 10758–10767.
- (15) Karahan, S.; Zahmakiran, M.; Özkaz, S. Catalytic methanolysis of hydrazine borane: a new and efficient hydrogen generation system under mild conditions. *Dalton Trans.* **2012**, *41*, 4912–4918.
- (16) Yao, Q.; Lu, Z.-H.; Zhang, Z.; Chen, X.; Lan, Y. One-pot synthesis of core-shell $Cu@SiO_2$ nanospheres and their catalysis for hydrolytic dehydrogenation of ammonia borane and hydrazine borane. *Sci. Rep.* **2014**, *4*, 7597.
- (17) Çakanyildirim, Ç.; Demirci, U. B.; Şener, T.; Xu, Q.; Miele, P. Nickel-based bimetallic nanocatalysts in high-extent dehydrogenation of hydrazine borane. *Int. J. Hydrogen Energy* **2012**, *37*, 9722–9729.
- (18) Chen, J.; Yao, Q.; Zhu, J.; Chen, X.; Lu, Z.-H. Rh–Ni nanoparticles immobilized on $Ce(OH)CO_3$ nanorods as highly efficient catalysts for hydrogen generation from alkaline solution of hydrazine. *Int. J. Hydrogen Energy* **2016**, *41*, 3946–3954.
- (19) Singh, S. K.; Zhang, X.-B.; Xu, Q. Room-temperature hydrogen generation from hydrous hydrazine for chemical hydrogen storage. *J. Am. Chem. Soc.* **2009**, *131*, 9894–9895.
- (20) Singh, S. K.; Xu, Q. Complete conversion of hydrous hydrazine to hydrogen at room temperature for chemical hydrogen storage. *J. Am. Chem. Soc.* **2009**, *131*, 18032–18033.
- (21) Wang, J.; Li, W.; Wen, Y.; Gu, L.; Zhang, Y. Rh–Ni–B nanoparticles as highly efficient catalysts for hydrogen generation from hydrous hydrazine. *Adv. Energy Mater.* **2015**, *5*, 1401879.
- (22) Hannauer, J.; Akdim, O.; Demirci, U. B.; Geantet, C.; Herrmann, J.-M.; Miele, P.; Xu, Q. High-extent dehydrogenation of hydrazine borane $N_2H_4BH_3$ by hydrolysis of BH_3 and decomposition of N_2H_4 . *Energy Environ. Sci.* **2011**, *4*, 3355–3358.
- (23) Zhong, D.-C.; Aranishi, K.; Singh, A. K.; Demirci, U. B.; Xu, Q. The synergistic effect of Rh–Ni catalysts on the highly-efficient dehydrogenation of aqueous hydrazine borane for chemical hydrogen storage. *Chem. Commun.* **2012**, *48*, 11945–11947.
- (24) Li, C.; Dou, Y.; Liu, J.; Chen, Y.; He, S.; Wei, M.; Evans, D. G.; Duan, X. Synthesis of supported Ni@RhNi-alloy nanocomposites as an efficient catalyst towards hydrogen generation from $N_2H_4BH_3$. *Chem. Commun.* **2013**, *49*, 9992–9994.

- (25) Zhu, Q.-L.; Zhong, D.-C.; Demirci, U. B.; Xu, Q. Controlled synthesis of ultrafine surfactant-free NiPt nanocatalysts toward efficient and complete hydrogen generation from hydrazine borane at room temperature. *ACS Catal.* **2014**, *4*, 4261–4268.
- (26) Cléménçon, D.; Petit, J. F.; Demirci, U. B.; Xu, Q.; Miele, P. Nickel- and platinum-containing core@shell catalysts for hydrogen generation of aqueous hydrazine borane. *J. Power Sources* **2014**, *260*, 77–81.
- (27) Zhang, Z.; Lu, Z.-H.; Tan, H.; Chen, X.; Yao, Q. CeO_x-modified RhNi nanoparticles grown on rGO as highly efficient catalysts for complete hydrogen generation from hydrazine borane and hydrazine. *J. Mater. Chem. A* **2015**, *3*, 23520–23529.
- (28) Zhang, Z.; Wang, Y.; Chen, X.; Lu, Z.-H. Facile synthesis of NiPt–CeO₂ nanocomposite as an efficient catalyst for hydrogen generation from hydrazine borane. *J. Power Sources* **2015**, *291*, 14–19.
- (29) Zhang, Z.; Lu, Z.-H.; Chen, X. Ultrafine Ni–Pt alloy nanoparticles grown on graphene as highly efficient catalyst for complete hydrogen generation from hydrazine borane. *ACS Sustainable Chem. Eng.* **2015**, *3*, 1255–1261.
- (30) Yao, Q.; Lu, Z.-H.; Jia, Y.; Chen, X.; Liu, X. In situ facile synthesis of Rh nanoparticles supported on carbon nanotubes as highly active catalysts for H₂ generation from NH₃BH₃ hydrolysis. *Int. J. Hydrogen Energy* **2015**, *40*, 2207–2215.
- (31) Yao, Q.; Lu, Z.-H.; Huang, W.; Chen, X.; Zhu, J. High Pt-like activity of the Ni–Mo/graphene catalyst for hydrogen evolution from hydrolysis of ammonia borane. *J. Mater. Chem. A* **2016**, *4*, 8579–8583.
- (32) Furukawa, H.; Cordova, K. E.; O’Keeffe, M.; Yaghi, O. M. The chemistry and applications of metal-organic frameworks. *Science* **2013**, *341*, 1230444.
- (33) Liu, H.; Chang, L.; Bai, C.; Chen, L.; Luque, R.; Li, Y. Controllable encapsulation of “Clean” metal clusters within MOFs through kinetic modulation: Towards advanced heterogeneous nanocatalysts. *Angew. Chem., Int. Ed.* **2016**, *55*, 5019–5023.
- (34) Jiang, H.-L.; Liu, B.; Akita, T.; Haruta, M.; Sakurai, H.; Xu, Q. Au@ZIF-8: CO oxidation over gold nanoparticles deposited to metal-organic framework. *J. Am. Chem. Soc.* **2009**, *131*, 11302–11303.
- (35) Jiang, H.-L.; Akita, T.; Ishida, T.; Haruta, M.; Xu, Q. Synergistic catalysis of Au@Ag core-shell nanoparticles stabilized on metal-organic framework. *J. Am. Chem. Soc.* **2011**, *133*, 1304–1306.
- (36) Zhu, Q.-L.; Li, J.; Xu, Q. Immobilizing metal nanoparticles to metal-organic frameworks with size and location control for optimizing catalytic performance. *J. Am. Chem. Soc.* **2013**, *135*, 10210–10213.
- (37) Yang, Q.; Xu, Q.; Yu, S.-H.; Jiang, H.-L. Pd nanocubes@ZIF-8: Integration of plasmon-driven photothermal conversion with a metal-organic framework for efficient and selective catalysis. *Angew. Chem., Int. Ed.* **2016**, *55*, 3685–3689.
- (38) Huang, G.; Yang, Q.; Xu, Q.; Yu, S.-H.; Jiang, H.-L. Polydimethylsiloxane coating for a palladium/MOF composite: Highly improved catalytic performance by surface hydrophobization. *Angew. Chem., Int. Ed.* **2016**, *55*, 7379–7383.
- (39) Chen, Y.-Z.; Wang, Z. U.; Wang, H.; Lu, J.; Yu, S.-H.; Jiang, H.-L. Singlet oxygen-engaged selective photo-oxidation over Pt nanocrystals/porphyrinic MOF: The roles of photothermal effect and Pt electronic state. *J. Am. Chem. Soc.* **2017**, *139*, 2035–2044.
- (40) Yang, Q.; Xu, Q.; Jiang, H.-L. Metal-organic frameworks meet metal nanoparticles: Synergistic effect for enhanced catalysis. *Chem. Soc. Rev.* **2017**, *46*, 4774–4808.
- (41) Férey, G.; Mellot-Draznieks, C.; Serre, C.; Millange, F.; Dutour, J.; Surlblé, S.; Margiolaki, I. A chromium terephthalate-based solid with unusually large pore volumes and surface area. *Science* **2005**, *309*, 2040–2042.
- (42) He, L.; Huang, Y.; Wang, A.; Wang, X.; Chen, X.; Delgado, J. J.; Zhang, T. A noble-metal-free catalyst derived from Ni-Al hydrotalcite for hydrogen generation from N₂H₄·H₂O decomposition. *Angew. Chem., Int. Ed.* **2012**, *51*, 6191–6194.
- (43) Jiang, Y.-Y.; Dai, H.-B.; Zhong, Y.-J.; Chen, D.-M.; Wang, P. Complete and rapid conversion of hydrazine monohydrate to hydrogen over supported Ni–Pt nanoparticles on mesoporous ceria for chemical hydrogen storage. *Chem. - Eur. J.* **2015**, *21*, 15439–15445.
- (44) Du, Y.; Su, J.; Luo, W.; Cheng, G. Graphene-supported nickel-platinum nanoparticles as efficient catalyst for hydrogen generation from hydrous hydrazine at room temperature. *ACS Appl. Mater. Interfaces* **2015**, *7*, 1031–1034.
- (45) Wang, H.-L.; Yan, J.-M.; Wang, Z.-L.; O, S.-I.; Jiang, Q. Highly efficient hydrogen generation from hydrous hydrazine over amorphous Ni_{0.9}Pt_{0.1}/Ce₂O₃ nanocatalyst at room temperature. *J. Mater. Chem. A* **2013**, *1*, 14957–14962.
- (46) Zhang, S. L.; Yao, Q. L.; Lu, Z. H. Synthesis and dehydrogenation of hydrazine borane. *Prog. Chem.* **2017**, *29*, 426–434.